



**HAL**  
open science

## Development of new biocompatible 3D printed graphene oxide-based scaffolds

Habib Belaïd, Sakthivel Nagarajan, Catherine Teyssier, Carole Barou, Jonathan Barés, Sébastien Balme, Hélène Garay, Vincent Huon, David Cornu, Vincent Cavailles, et al.

### ► To cite this version:

Habib Belaïd, Sakthivel Nagarajan, Catherine Teyssier, Carole Barou, Jonathan Barés, et al.. Development of new biocompatible 3D printed graphene oxide-based scaffolds. *Materials Science and Engineering: C*, 2020, 110, pp.110595. 10.1016/j.msec.2019.110595 . hal-02477859

**HAL Id: hal-02477859**

**<https://hal.science/hal-02477859v1>**

Submitted on 13 Feb 2020

**HAL** is a multi-disciplinary open access archive for the deposit and dissemination of scientific research documents, whether they are published or not. The documents may come from teaching and research institutions in France or abroad, or from public or private research centers.

L'archive ouverte pluridisciplinaire **HAL**, est destinée au dépôt et à la diffusion de documents scientifiques de niveau recherche, publiés ou non, émanant des établissements d'enseignement et de recherche français ou étrangers, des laboratoires publics ou privés.

# Development of new biocompatible 3D printed graphene oxide-based scaffolds

Habib Belaid<sup>a,b</sup>, Sakthivel Nagarajan<sup>a</sup>, Catherine Teyssier<sup>b</sup>, Carole Barou<sup>a,b,c</sup>, Jonathan Barés<sup>d</sup>,  
Sebastien Balme<sup>a</sup>, Hélène Garay<sup>d</sup>, Vincent Huon<sup>d</sup>, David Cornu<sup>a</sup>, Vincent Cavallès<sup>a,1</sup>,  
Mikhael Bechelany<sup>a,\*,1</sup>

<sup>a</sup> Institut Européen des Membranes, IEM – UMR 5635, ENSCM, CNRS, Univ Montpellier, Montpellier, France

<sup>b</sup> IRCM, Institut de Recherche en Cancérologie de Montpellier, INSERM U1194, Université Montpellier, Montpellier F-34298, France

<sup>c</sup> Biologics 4 life, 84120 Pertuis, France

<sup>d</sup> LMGC, Laboratoire de Mécanique et Génie Civil, Univ Montpellier, CNRS, Montpellier, France

<sup>e</sup> C2MA, IMT mines d'Alès, France

## A B S T R A C T

The aim of this work was to develop a bioresorbable, biodegradable and biocompatible synthetic polymer with good mechanical properties for bone tissue engineering applications. Polylactic acid (PLA) scaffolds were generated by 3D printing using the fused deposition modelling method, and reinforced by incorporation of graphene oxide (GO). Morphological analysis by scanning electron microscopy indicated that the scaffold average pore size was between 400 and 500  $\mu\text{m}$ . Topography imaging revealed a rougher surface upon GO incorporation ( $S_a = 5.8 \mu\text{m}$  for PLA scaffolds, and of  $9.9 \mu\text{m}$  for PLA scaffolds with 0.2% GO), and contact angle measurements showed a transition from a hydrophobic surface (pure PLA scaffolds) to a hydrophilic surface after GO incorporation. PLA thermomechanical properties were enhanced by GO incorporation, as shown by the  $70^\circ\text{C}$  increase of the degradation peak (thermal gravimetric analysis). However, GO incorporation did not change significantly the melting point assessed by differential scanning calorimetry. Physicochemical analyses by X-ray diffraction and Raman spectroscopy confirmed the filler presence. Tensile testing demonstrated that the mechanical properties were improved upon GO incorporation (30% increase of the Young's modulus with 0.3%GO). Cell viability, attachment, proliferation and differentiation assays using MG-63 osteosarcoma cells showed that PLA/GO scaffolds were biocompatible and that they promoted cell proliferation and mineralization more efficiently than pure PLA scaffolds. In conclusion, this new 3D printed nanocomposite is a promising scaffold with adequate mechanical properties and cytocompatibility which may allow bone formation.

### Keywords:

Polylactic acid  
Graphene oxide  
Nanocomposite  
3D printing  
Biocompatibility

## 1. Introduction

For decades, bone disease management, for instance in osteoporosis, has been challenging due to the reduced bone self-repair capacity [1]. Therefore, in patients with critical bone loss, fractures are treated by surgical implantation of a passive artificial junction called “scaffold”, used to promote bone growth [2]. In this approach, the scaffold morphology, chemical composition and physico-chemical properties play key roles because they must mimic the multi-scale structure of the bone extracellular matrix to allow cell adhesion, proliferation and differentiation [3,4]. The scaffold mechanical properties, degradation and biocompatibility are directly influenced by the composition of the used

material [5].

To fabricate biomaterials suitable for bone regeneration, formulations based on biodegradable polylactic acid (PLA) polymers [6] have been developed. PLA is made of dextrose extracted from bio-based materials, such as corn or cellulose [7]. It is routinely used for medical applications, for instance in sutures [8] or orthopaedic fixation devices [9]. Unfortunately, biodegradable synthetic materials, such as PLA, are rather brittle and usually display relatively small deformation at break, high rigidity, and low plasticity for small deformations. These mechanical characteristics (e.g., Young's modulus of about 2–3 GPa and ultimate strength of 53 MPa [10] for bulk material) are often incompatible with biological applications. Specifically, cortical bone has

\* Corresponding author.

E-mail address: [mikhael.bechelany@umontpellier.fr](mailto:mikhael.bechelany@umontpellier.fr) (M. Bechelany).

<sup>1</sup> Co-last authors.

a modulus of elasticity between 7 and 17 GPa and an ultimate strength up to 133 MPa, depending on the age. In trabecular bone, the elastic modulus is about 0.44 GPa and the ultimate strength is 6.8 MPa [11]. Moreover, PLA hydrophobicity renders bone cell attachment and proliferation difficult [12].

To overcome these problems, PLA scaffold properties could be improved by incorporating nanofillers, such as graphene oxide (GO) [13]. Graphene (the elementary structure of graphite) is a single layer sheet composed of sp<sup>2</sup>-bonded carbon atoms arranged in a flat honeycomb structure. It possesses remarkable properties, such as high mechanical strength and extremely large surface area [14,15]. GO structure is similar with the addition of polar functional groups (such as epoxides, hydroxyl, carboxylic groups) that are crucial for promoting interaction with the polymer matrix [16,17]. Different studies have investigated PLA reinforcement with GO [18,20]. For example, Pinto et al. showed that GO addition increases the Young's modulus by 115% and the yield strength by 95% [19]. Other studies demonstrated that GO reinforcement of biopolymers is biocompatible, promotes cell adhesion and proliferation, and improves composite wetting [21–25].

To design scaffolds for bone tissue engineering, different synthesis techniques can be used: solvent casting and particulate leaching [26], emulsion freeze-drying [27], phase separation [28], or electrospinning [29]. However, these techniques do not allow controlling efficiently the morphology and structure of the interconnected pores. On the other hand, various studies demonstrated that the 3D controlled scaffold architecture significantly affects its mechanical properties [30,31] as well as bone cell adhesion and proliferation [32,33]. Therefore, recent works focused on the development of 3D printed scaffolds [34–36] using different techniques, such as stereolithography [37,38], 3D plotting [39], selective laser sintering [40], bioprinting [41], and fused deposition modelling (FDM) [42]. FDM is the most widely used additive manufacturing method and presents several advantages compared with other techniques [43]. Indeed, FDM is cheap, does not require solvents, and gives great possibilities in polymer handling and processing [44]. Amorphous thermoplastic polymers, such as PLA, are among the most common materials used in this type of process [45–47].

The objective of this work was to create a 3D porous scaffold with controlled architecture, good mechanical properties and adequate composition allowing biocompatibility. To this aim, we developed a PLA/GO nanocomposite material and created by FDM 3D printing a multifunctional scaffold with a customized structure. We then analysed many parameters of these scaffolds (morphology, chemical, structural and mechanical properties, and biocompatibility) to demonstrate their potential usefulness for biological applications.

## 2. Experimental section

### 2.1. Materials

PLA pellets were purchased from NatureWorks LLC. Graphite powder (20 µm synthetic, CAS 7782-42-5), dichloromethane (CH<sub>2</sub>Cl<sub>2</sub>, < 99.9%, CAS 75-09-2), sulfuric acid (H<sub>2</sub>SO<sub>4</sub>, 95.0–98.0%, CAS 7664-93-9), phosphoric acid (H<sub>3</sub>PO<sub>4</sub>, 85 wt% in H<sub>2</sub>O, CAS 7664-38-2), hydrogen peroxide (H<sub>2</sub>O<sub>2</sub>, 30% (w/w), CAS 7722-84-1), potassium permanganate (KMnO<sub>4</sub>, > 99.0%, CAS 7722-64-7), ethanol (96% vol, CAS 64-17-5), cetylpyridinium chloride (CAS 6004-24-6), glutaraldehyde (25% in H<sub>2</sub>O, CAS 111-30-8), 37% formaldehyde (37 wt % in H<sub>2</sub>O, CAS 50-00-0), phosphate buffered saline (PBS) (P4417) tablets, Triton X 100 (CAS 9002-93-11), Bovine Serum Albumin (BSA) (≥ 98%, CAS 9048-46-8), Mowiol 40–88 (CAS 9002-89-5), L-ascorbic acid (CAS 50-81-7), β-glycerophosphate (≥ 99%, CAS 154804-51-0), Alizarin Red S (CAS 130-22-3), anti-actin antibody (clone CA15, A5441), dexamethasone (≥ 80%, CAS 50-02-2), Hoechst 33342 (≥ 98%, CAS 23491-52-3) and 3-(4,5-dimethylthiazol-2-yl)-2,5-diphenyl tetrazolium bromide (MTT, 98%, CAS 298-93-1) were purchased from Sigma-Aldrich. Acetone (≥ 99% (GC), CAS 67-64-1) was

purchased from Honeywell. Tween 20 (CAS 9005-64-5) was purchased from VWR International. Alexa-conjugated anti mouse IgG (Alexa fluor 488, A11001) was purchased from ThermoFisher Scientific. MEM alpha medium (Gibco 12571-063), dimethyl sulfoxide (DMSO) (BDH Prolabo 23486.297), foetal bovine serum (FBS) (Eurobio CVFVSF00-01), penicillin/streptomycin (Gibco 15140-122) and 0.05% trypsin-EDTA (Gibco 25300-054) were used for cell cultures.

### 2.2. Preparation of the PLA/GO scaffolds

GO was prepared according to the modified Hummers method [48]. Briefly, 3 g of graphite powder was added to a 9:1 mixture of concentrated H<sub>2</sub>SO<sub>4</sub>/H<sub>3</sub>PO<sub>4</sub> under stirring for 5 min. Then, 18 g of KMnO<sub>4</sub> was added to the solution containing the graphite and the acid mixture, and stirred for 12 h. Then, 3 mL of H<sub>2</sub>O<sub>2</sub> was added to the solution with magnetic stirring for 1 h, followed by centrifugation at 6000 rpm for 10 min. The precipitates were first washed with 30% HCl, then with distilled water, and finally with ethanol. The purified GO precipitate was dried at 50 °C for 24 h.

The PLA solution (10 mL of 10% (w/v)) was prepared using dichloromethane as solvent. Different percentages of filler (0.1 to 0.3 wt %) were used. GO was dispersed in acetone (1 mg per mL) and placed in an ultrasonic bath for 15 min. The GO-containing solution was added to the polymer solution under constant magnetic stirring until the solution was homogeneous. The composite polymer solution was poured into a Teflon dish and allowed to dry at room temperature overnight. The obtained dried polymer was a film and was cut into pieces and introduced into a single screw extruder (Noztek pro) at an extrusion temperature of 200 °C. A filament with a diameter of 1.75 mm was obtained and used for 3D printing. The scaffold was modelled using computer-aided design (CAD) software (Design Spark Mechanical). After deciding the scaffold shape, a STL file was created to be analysed with the Prusa3D slicer software. Scaffolds were 3D printed using a Prusa Research MK2S printer. All printing parameters are given in Table S1.

### 2.3. Morphological properties

The scaffold size, morphology, and microstructure were analysed by scanning electron microscopy (SEM) (HITACHI S4800 system). For SEM observation, scaffolds were coated with platinum using a Polaron SC7620 Mini Sputter Coater. The diameters of the struts and of the obtained pores were calculated with the Image J software.

A chromatic confocal rugosimeter (STIL SA) equipped with a CHR1000 sensor was used for the 3D characterization of the topography of cylinder surface areas of 10 mm of 3D printed PLA and PLA/GO scaffolds (two different locations of 2 \* 2 mm for each scaffold with 5 lateral µm step). Data post-treatment was done with MountainsMap7 (DigitalSurf). The determined roughness parameter was the arithmetical mean height of the surface (Sa).

The contact angles of ultrapure water on 3D printed PLA and PLA/GO scaffolds was measured using the sessile drop method with a B-CAM-21-BW (CCCIR) monochrome camera and a Led R60 lamp (Conrad). Equilibrium contact angles (considered at 60s) were measured for 5 µL droplet volumes in three different locations for each condition. One Touch Grabber and Image J were used to calculate the contact angles.

### 2.4. Chemical and structural properties

Raman spectra of scaffolds and films were obtained in ambient conditions using a 659.55 nm laser and a Horiba Jobin Yvon Raman spectrometer (model M.F.O). The X-ray diffraction (XRD) patterns of PLA and PLA/GO scaffolds were recorded using CuKα radiation, 2θ range of 10–70° with a scan speed of 2°·min<sup>-1</sup>, and the PANalytica Xpert powder XRD system. The Fourier Transform Infrared (FTIR)

spectrum of PLA and PLA/GO nanocomposites was recorded with the NEXUS instrument, equipped with an attenuated total reflection accessory in the frequency range of 600–4000  $\text{cm}^{-1}$ . The FTIR spectrum was scanned at 1  $\text{cm}^{-1}$  resolution, and signals were averaged from 32 scans.

## 2.5. Thermal properties

The different scaffolds were analysed using a differential scanning calorimeter 2920 (maker), equipped with a RCS90 cooling system (maker). Samples were accurately weighed ( $\approx 4$  mg) in an aluminium TA pan (maker) and sealed. An empty sealed pan was used as reference. Samples were first cooled to 25  $^{\circ}\text{C}$  and then heated to 210  $^{\circ}\text{C}$  with a heating rate of 10  $^{\circ}\text{C min}^{-1}$ . Then, they were cooled again to 25  $^{\circ}\text{C}$  with nitrogen as purge gas. The degree of polymer crystallinity was calcu-

lated  $\chi = \frac{\Delta H_f - \Delta H_{cf}}{\Delta H_{\infty}}$  where  $\Delta H_f$  is the enthalpy of fusion,  $\Delta H_{cf}$  is the enthalpy of cold crystallization, and  $\Delta H_{\infty}$  is the reference melting enthalpy for the 100% crystalline polymer ( $\Delta H_{\infty} = 93 \text{ J}\cdot\text{g}^{-1}$ ) [49]. The resulting differential scanning calorimetry (DSC) curves were analysed to determine the polymer glass transition temperature ( $T_g$ ), the melting temperature ( $T_m$ ), the cold temperature crystallization ( $T_{cc}$ ) and the crystallinity ( $X_c$ ). The thermogravimetric analysis (TGA) was performed using a TGA G500 device (TA Instruments). About 10 mg of each sample was heated in air atmosphere from room temperature to 900  $^{\circ}\text{C}$ , at a heating rate of 10  $^{\circ}\text{C}\cdot\text{min}^{-1}$ .

## 2.6. Mechanical properties

The mechanical properties of the 3D printed PLA/GO scaffolds were characterized using a modular traction system (1/ME) coupled with a 5 kN force sensor (maker). Samples were printed in the shape of a dog bone (40 mm length, 4 mm width, and 1.5 mm thick). The exact geometry is given in Fig. S1. Samples were then clamped between dedicated jaws and pulled at a constant speed of 0.01  $\text{mm}\cdot\text{s}^{-1}$  until they broke. Samples were imaged with a 16 Mb camera (SVS-VISTEK) at 1 Hz. Samples were initially randomly patterned with thin black paint to perform digital image correlation (DIC). Using an already described DIC algorithm dedicated to large deformations [50,51], sample strain changes could be computed without inaccuracy coming from the machine and jaw plays. Linear elastic regions from the stress–strain graphs were then used to calculate the Young's modulus from at least three assays. The stress at which the sample begins to break was also measured.

## 2.7. Biodegradation

The enzymatic degradation of PLA and PLA/GO(0.2%) by alcalase was monitored during 25 days following a previously reported method for biodegradation analysis [52]. Briefly, PLA and PLA/GO strips were printed (50 [w]  $\times$  150 [l]  $\times$  0.126 [h] mm, approximately 0.5 g) and immersed in 25 mL of TRIS buffer (pH 9.5, 60  $^{\circ}\text{C}$ ) with 3 mM L-cysteine, 0.05% sodium azide and 50% on weight of fabric enzyme concentration. Weight loss of the nanocomposites was evaluated by determining the dry weight of the samples at 4, 18 and 25 days. The samples were dried at 105  $^{\circ}\text{C}$  for 90 min, cooled in a desiccator, and then weighed in a closed weighing bottle. The percentage weight loss was calculated as follows: Weight loss (%) =  $(W_1 \times W_2/W_1) \times 100$  where  $W_1$  and  $W_2$  are the dry weights of the samples before and after biodegradation, respectively.

## 2.8. Cell viability and adhesion assays

Scaffolds were sterilized with ethanol for 30 min and under UV light (405 nm) for 1 h. MG-63 osteosarcoma cells and MC3T3-E1 pre-osteoblast cells were cultured on the sterilized scaffolds for 7 days. Cell

viability was analysed using the MTT assay. Cells were incubated with 100  $\mu\text{L}$  of culture medium containing 0.05  $\text{mg}\cdot\text{mL}^{-1}$  of MTT solution for 3 h. The obtained purple-coloured formazan crystals, due to MTT reduction by living cells, were solubilized by addition of 100  $\mu\text{L}$  of DMSO and absorbance recorded at 560 nm using a Multiskan microplate spectrophotometer (ThermoFisher, USA). For the cell adhesion assay, MG-63 cells were fixed with 4% formaldehyde (500  $\mu\text{L}$  per well) at room temperature for 20 min. After washing with PBS and permeabilization with PBS/0.1% Triton X 100 for 15 min, cells were incubated with PBS/1% BSA for 3 h. Then, they were incubated with an anti-actin antibody (to stain the cytoskeleton) at 4  $^{\circ}\text{C}$  overnight, and washed twice with PBS/0.05% Tween 20. After incubation with the Alexa-conjugated anti mouse IgG secondary antibody, nuclei were stained with Hoechst 33342 at room temperature for 1 h. Samples were mounted with Mowiol and images acquired with a fluorescent microscope (DM6000 Leica).

## 2.9. Mineralization assay

MG-63 cells were plated in Petri dishes on the PLA/GO nanocomposites and grown until confluence (day 0). Then, they were switched to differentiation medium, supplemented with ascorbic acid (50  $\text{mg}\cdot\text{mL}^{-1}$ ),  $\beta$ -glycerophosphate (5 mM) and dexamethasone ( $10^{-8}$  M) that was refreshed every 48 h. Mineralized nodule formation was monitored at day 0, 14 and 21 by staining with Alizarin Red-S. Briefly, cells were rinsed twice with PBS and fixed with 4% formaldehyde at room temperature for 20 min. Then, cells were rinsed twice with PBS (pH 4.2), and stained with 40 mM Alizarin Red-S (pH 4.2) at room temperature for 20 min, followed by extensive rinsing with water. For quantification, the supernatant absorbance was measured at 540 nm using a microplate reader (Bio-Rad) after extraction with 10% (wt/vol) cetylpyridinium chloride. The background level of OD obtained in the absence of any cells was subtracted from all measurements.

## 2.10. Statistical analysis

All the results are described as means  $\pm$  standard deviation (SD). The statistical significance between groups were determined with the Student's *t*-test and were considered significant for \* $p < 0.05$  and \*\* $p < 0.005$ .

## 3. Results and discussion

### 3.1. Generation and morphological analysis of PLA/GO scaffolds

To reinforce PLA, GO fillers were added to the polymer matrix at different percentages (0.1, 0.2, and 0.3%) and named PLA/GO-films. The composites were then extruded via a single screw extruder and put in shape with a FDM system. To facilitate bone regeneration, it was decided to generate scaffolds with a porous interconnected network and a pore size around 300  $\mu\text{m}$ , corresponding to an infill of 70% (see Table S1 for the used printing parameters and Fig. S2 for macroscopic images of the scaffolds).

The SEM micrographs shown in Fig. 1 illustrate the porous morphology of scaffolds obtained with PLA alone (Fig. 1a) or with 0.2% GO (Fig. 1b). The pore size ( $405 \pm 20 \mu\text{m}$  and  $485 \pm 30 \mu\text{m}$ , respectively) and the wall width ( $380 \pm 65 \mu\text{m}$  and  $360 \pm 130 \mu\text{m}$ , respectively) were comparable in the PLA scaffolds and in the PLA scaffolds with 0.2% of GO. Similar results were obtained with 0.1% and 0.3% GO (Table 1), showing that GO addition in the PLA matrix had a very moderate effect on pore morphology during the 3D printing step.

Analysis of the 3D topography images (Fig. 2) indicated that the surface of PLA scaffolds with 0.2% GO (Fig. 2b) was rougher compared with the smooth surface of PLA scaffolds (Fig. 2a). In agreement, PLA scaffolds with 0.2% GO displayed higher  $S_a$  values (Table 1). This could

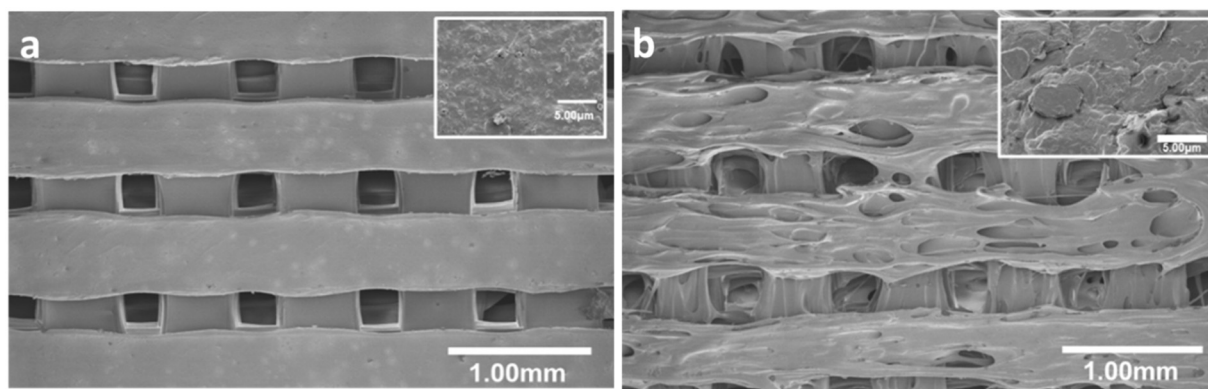


**Fig. 1.** Scanning electron micrographs showing the architecture of FDM 3D printed (a) PLA and (b) PLA/GO (0.2%) scaffolds. Insets show a magnification of the surface.

be attributed to the presence of fillers at the surface and their good dispersions in the polymer matrix [53]. Only in PLA scaffolds with 0.3% GO, roughness was slightly decreased compared with PLA scaffolds (Table 1), and this could be due GO agglomeration.

In bone tissue engineering, the surface properties of biomedical devices are very important. For instance, the material must display sufficient hydrophilicity to allow the attachment of cells on the scaffold surface, and their proliferation and differentiation for bone regeneration [54–56]. Water contact angles (Fig. S3) were smaller for PLA/GO scaffolds compared with PLA scaffolds (Table 1). Pinto et al. [18] reported similar results for PLA/GO films with a decrease of the contact angle of about 9° after GO addition. Conversely, Zhang et al. found that GO addition had no effect on the contact angle for PLA/GO electrospun fibers [57]. This suggests that GO presence at the scaffold surface increases its hydrophilicity, and that the method used to obtain the final material directly influences the surface properties. In our study, pristine PLA had a contact angle of 118°, while PLA with 0.3% of GO had a contact angle of 54°. This reduction might be caused by direct interactions of the liquids with partially exposed fillers at the PLA surface. Hydrogen bond interactions between oxygen-containing groups in GO and water can explain this behavior. In conclusion, the presence of GO in the 3D PLA matrix decreased the surface hydrophobic properties and, as a consequence, should improve cell attachment and proliferation at the surface of the material.

### 3.2. Structural characterization of PLA/GO scaffolds

To confirm GO formation from graphite, XRD analysis of the obtained powder showed the characteristic GO peak at 11° that corresponded to the (002) plane (Fig. 3a). This evidenced graphite exfoliation through the oxidation process. The PLA-film (red in Fig. 3a) showed four characteristic peaks at  $2\theta = 15, 17, 19$  and  $23^\circ$  that described the alpha form of PLA [58]. PLA crystalline peaks disappeared after filament extrusion (green). This might be due to the quenching (air atmosphere) of PLA melting during 3D printing and the high speed of cooling that inhibited the crystalline structure rearrangement. Moreover, it has been shown that natural PLA has the lowest percentage of crystallinity among PLA filaments (coloured or not) [59]. Hence, the XRD results suggest that PLA crystalline phase was lost during

extrusion.

The PLA/GO biocomposites before extrusion (PLA/GO-film; blue in Fig. 3a) displayed two characteristic PLA peaks at  $2\theta = 17$  and  $23^\circ$ . However, these peaks were broader than in the PLA-film, possibly due to micro-stresses induced by GO addition in the polymer matrix. Indeed, the peak corresponding to GO was not detected. This could be related to the low percentage of fillers or the good GO dispersion in the matrix [60]. After extrusion, the same behavior was observed for the PLA/GO scaffold (pink, Fig. 3a), with a broad peak between  $10^\circ$  and  $25^\circ$  that corresponded to the polymer amorphous nature.

### 3.3. Chemical characterization of the scaffolds

To understand PLA organization and GO interactions with the polymer matrix during the nanocomposite fabrication, FTIR spectra were recorded (Fig. 3b). The characteristic GO functions were the bands at  $1040\text{ cm}^{-1}$  (C–O elongation vibrations) and  $1740\text{ cm}^{-1}$  (C=O elongation vibrations of the carbonyl and carboxylic groups). The peak at  $1630\text{ cm}^{-1}$  was probably due to skeletal vibration of the graphite domains. The broad peak around  $3000\text{--}3500\text{ cm}^{-1}$  was attributed to hydroxyl groups. No difference was observed between the peaks of pure PLA and PLA/GO scaffolds. Indeed, the greater PLA peak absorbance and in the same range than that of GO did not allow detecting the GO peaks in the PLA/GO biocomposites.

Similarly, the D and G-band signature of pure GO powder was detected at  $1345$  and  $1590\text{ cm}^{-1}$  respectively, using Raman spectroscopy (Fig. 3c). The vibration of sp<sup>2</sup>-bonded carbon atoms in a 2D hexagonal lattice gave the G-band, whereas the vibration of carbon atoms with pendent bonds in the plane of the disordered graphite was associated with the D band. The D band is generally correlated with defects from vacancies, grain boundaries, and amorphous carbon species that lead to sp<sup>3</sup>-hybridized carbon, hence a differentiated band of sp<sup>2</sup>-hybridized carbon. For the PLA/GO film, two peaks were observed at  $1345$  and  $1590\text{ cm}^{-1}$  that appeared as widened bands of weak intensities and corresponded to the presence of GO in the PLA. The Raman spectra of PLA/GO scaffolds were not significantly different from those of PLA scaffolds.

**Table 1**

Pore size, wall width, roughness (*i.e.*, Sa, the arithmetic average height of the surface), and contact angles of ultrapure water for PLA and PLA/GO scaffolds.

Samples	Pore size (µm)	Wall width (µm)	Sa (µm)	Contact angles (°)
PLA	405 ± 20	380 ± 65	5.8 ± 1.5	118 ± 2
PLA/GO (0.1%)	450 ± 25	350 ± 100	7.5 ± 0.6	70 ± 2
PLA/GO (0.2%)	485 ± 30	360 ± 130	9.9 ± 4.0	69 ± 1
PLA/GO (0.3%)	455 ± 24	400 ± 130	5.5 ± 0.9	54 ± 2

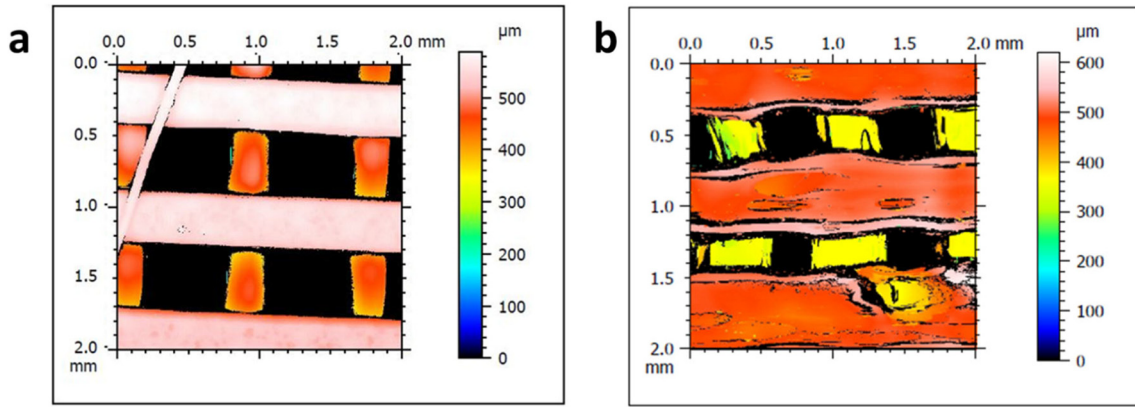


Fig. 2. Scaffold topography. Representative 3D images of the surface roughness of (a) PLA and (b) PLA/GO (0.2%) scaffolds.

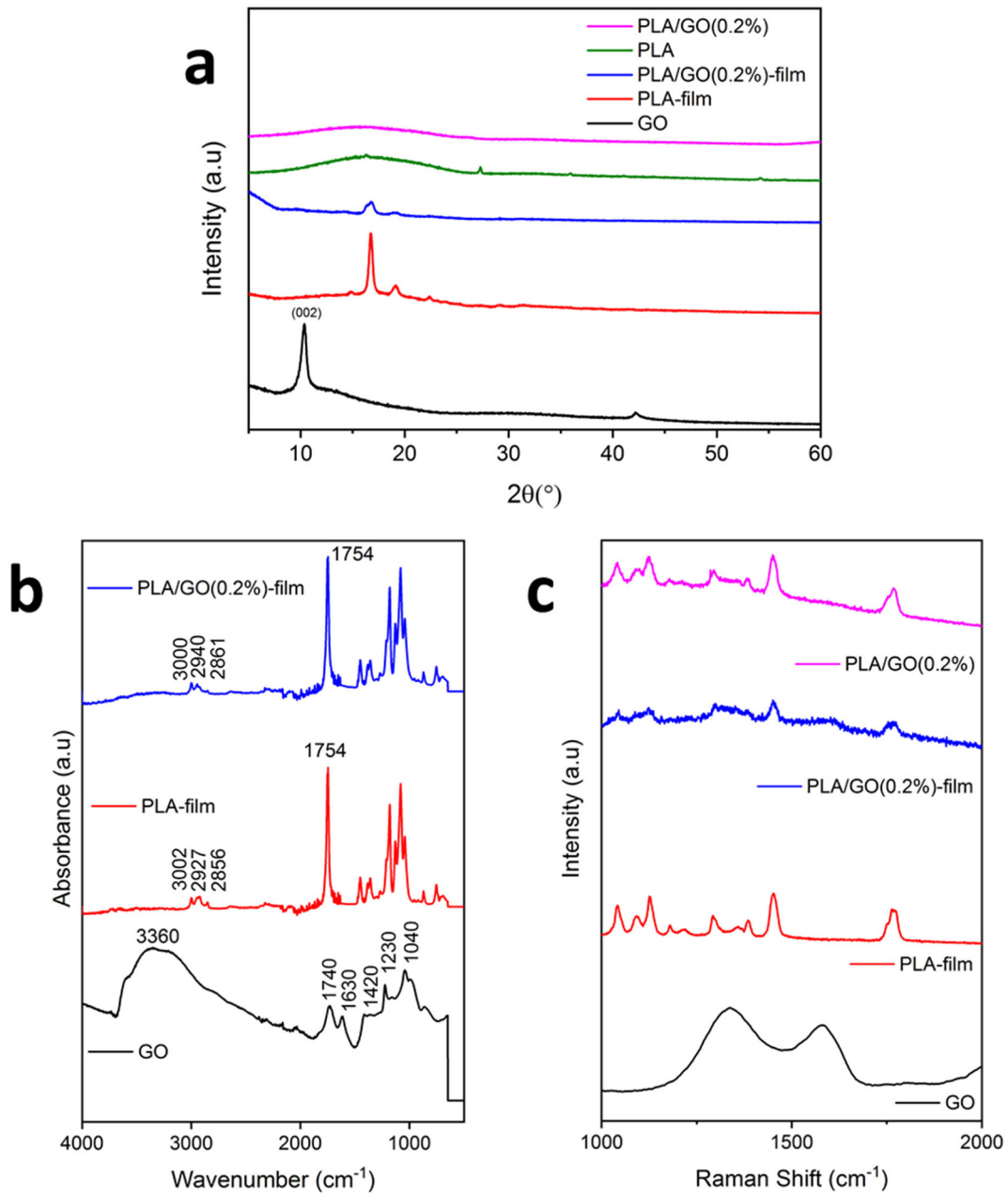
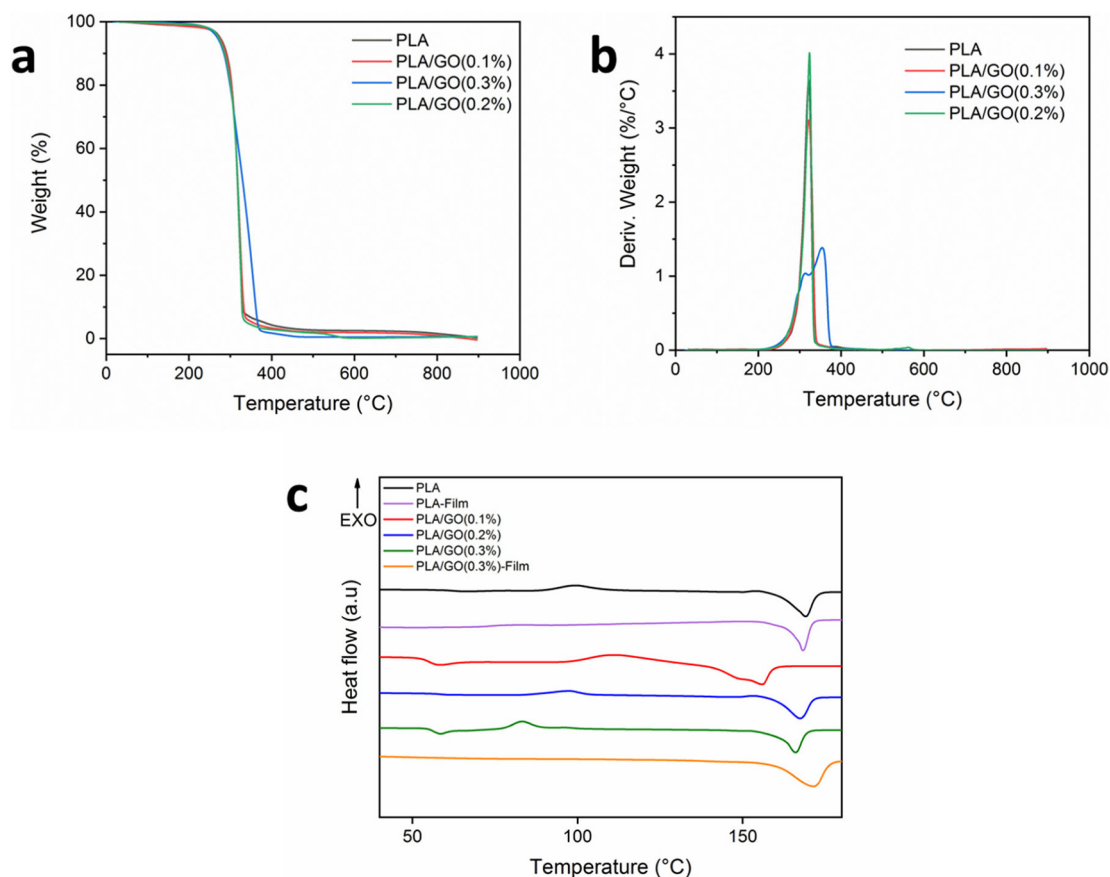


Fig. 3. Chemical and structural properties of the nanocomposites. (a) XRD diffractograms, (b) FTIR spectra, and (c) Raman spectroscopy data of the synthesized GO and PLA/GO nanocomposites (films or 3D printed scaffolds, as indicated).



**Fig. 4.** Thermal properties of nanocomposite materials. (a) TGA and (b) derivative TGA curves of 3D printed PLA nanocomposites with different GO percentages. (c) Representative DSC graphs showing Tg (glass transition temperature), Tm (melting temperature) and Tcc (cold temperature crystallization) of PLA and PLA/GO nanocomposites before and after 3D printing.

### 3.4. Thermal analysis of the PLA/GO scaffolds

The influence of GO on PLA thermal stability was monitored by TGA (Fig. 4a). The 1% weight loss for PLA observed below 200 °C was due to the adsorbed water. The second major weight loss observed between 300 and 400 °C was caused by the degradation of the PLA polymer. As shown in the derivative weight curves (Fig. 4b), the maximum degradation temperature peak shifted from 298 °C to 366 °C for the nanocomposites with 0.3% GO. This shift could be explained by the interfacial interactions between GO and PLA through hydrogen bonds and/or van der Waals forces, as previously reported [61,62]. The strong interactions with GO led to the improvement of the biocomposite thermal stability, possibly due to a diminution of the chain mobility at the interface with GO [63]. The last weight loss from 400 °C was due to the thermochemical decomposition of the remaining organic content from PLA and from GO due to pyrolysis of labile oxygenated groups when PLA is reinforced with GO [64].

The effects of GO addition on PLA crystallinity and on Tg, Tcc and Tm were evaluated by DSC analyses (Fig. 4c). Enthalpy of fusion, glass transition and melting point were measured and are summarized in Table 2, together with the calculated crystallinity. For PLA, Tg were 59 °C and 61 °C and Tm were 168 °C and 169 °C before and after extrusion, respectively. This indicated that the extrusion process did not affect PLA thermal properties.

After extrusion, PLA showed a cold crystallization peak at 100 °C. Conversely, the cold crystallization peak was suppressed before extrusion, as reported in a previous study on a PLA film [65]. In line with these observations, PLA crystallinity level was lower after than before extrusion, and this change could have been caused by the extrusion process [66]. These results confirmed the XRD observations on the

**Table 2**

Temperatures, enthalpies of different thermal transitions, and crystallinity of PLA and PLA/GO materials.

Samples	Tg (°C)	Tm(°C)	ΔHf (J/g)	ΔHcf (J/g)	χ (%)
PLA	61	169	30	10	21
PLA-film	59	168	30	-	32
PLA/GO (0.1%)	55	156	27	27	0
PLA/GO (0.2%)	57	171	43	19	26
PLA/GO (0.3%)	56	166	40	24	16
PLA/GO (0.3%)-film	55	169	42	-	45

Tg, glass transition temperature; Tm, melting temperature; ΔHf, enthalpy of fusion; ΔHcf, enthalpy of cold crystallization; χ, crystallinity.

polymer crystallinity changes during extrusion.

For PLA reinforced with 0.1% GO, the glass transition at 55 °C was followed by an exothermic cold crystallization peak at 112 °C. When the GO content was increased to 0.3%, the Tg at 56 °C was followed by a double peak of cold crystallization at 83 °C. These results are surprising because a previous study reported that the Tg of graphene and GO/polymer nanocomposites is significantly increased (4 °C or more) when using functionalized nanofillers, due to more interactions with the matrix [67]. Moreover, GO addition should increase the cold crystallization temperature because in the presence of enough GO content in the polymer matrix, the motion of PLA chains is confined, the cold crystallization process of PLA is restricted, and consequently the crystallization temperature increases [68].

The melting peak was not changed by GO addition to the PLA matrix, but a double melting peak appeared at 166 °C when GO loading level was increased to 0.3 wt%. The second melting peak was higher,

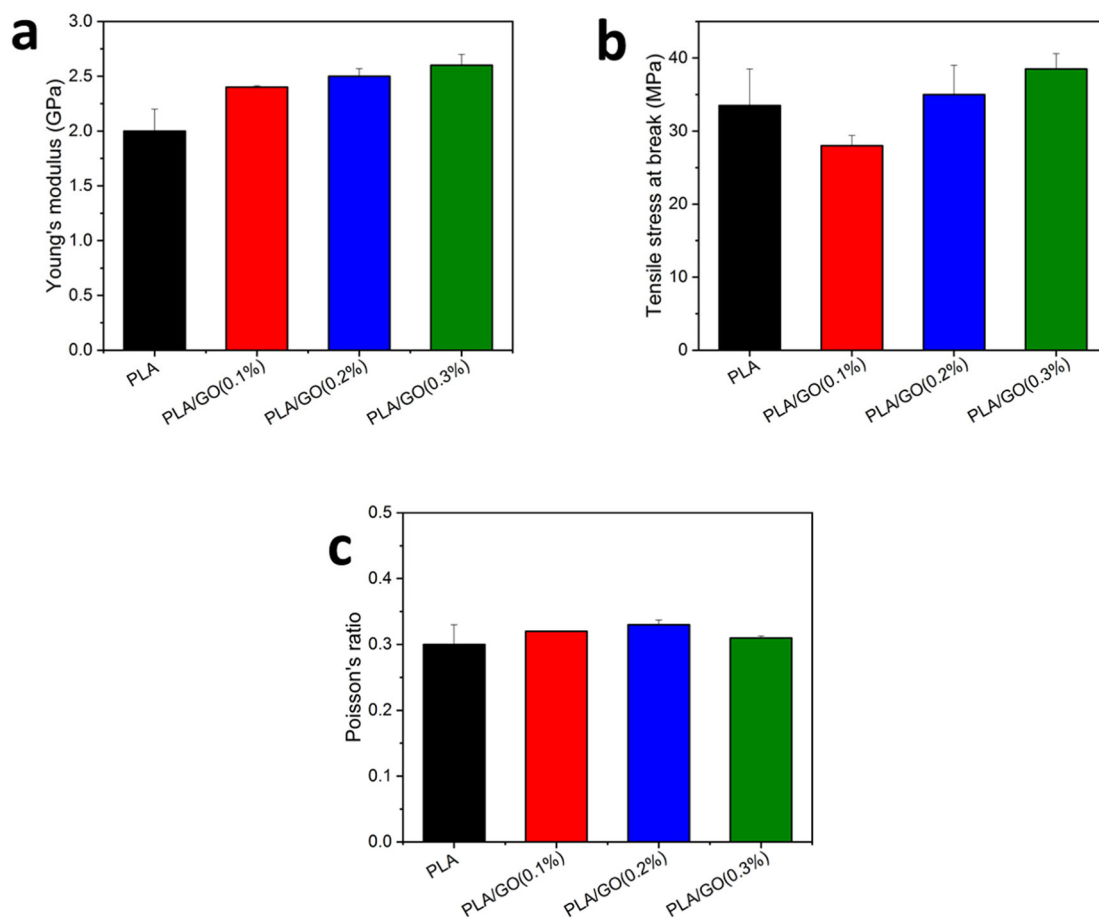


Fig. 5. Mechanical properties of the scaffolds. (a) Young's modulus, (b) Tensile stress at break, and (c) Poisson's ratio values of the different PLA/GO scaffolds compared with PLA scaffolds.

indicating that more crystalline forms were generated with higher GO loading levels [69]. Finally, thermal analysis by TGA and DSC showed that GO presence in the polymer matrix did not affect the filament extrusion. The 3D printing conditions also were not influenced by GO addition. However, GO enhanced the thermal stability of the nanocomposite scaffolds.

### 3.5. Mechanical properties of the 3D printed nanocomposites

Composites used for biomedical implants should withstand high tensile loads. The characterization of the mechanical properties of PLA and PLA/GO nanocomposites (Fig. 5) focused on the region where samples responded elastically to traction. In this region, the elastic modulus was measured as a function of the GO percentage. The Young's modulus for PLA was in good agreement with the literature [70] (i.e., about 2 GPa for a sample with 30% porosity). This value significantly increased to 2.6 GPa after addition of 0.3% GO (improvement of about 30% of the elastic modulus) for a scaffold with 30% porosity (Fig. 5a).

Then, samples were loaded until breaking. When GO density was high enough, GO incorporation increased the tensile strength from 34 MPa for pure PLA to 39 MPa for samples with 0.3% GO. Conversely, in samples with lower GO density, tensile strength at break was lower (Fig. 5b). This is due to the fact the GO induced flaws at the very local scale that made the material weaker. With higher GO densities, this phenomenon is counterbalanced by the fact that GO is intrinsically stronger than PLA, which makes the material stronger. The Poisson's ratio was 0.3 for PLA, which is characteristic for this polymer, and was not changed by GO addition (Fig. 5c). The improved stiffness of the PLA/GO scaffold compared with the PLA scaffold highlighted the

reinforcement of the scaffold by GO addition.

Here, only the influence of GO addition on the polymer mechanical properties was investigated. However, the architecture and percentage of filling inside the scaffold also have an effect on the mechanical properties of the material, particularly on the tensile strength, but these features were beyond the goal of this study.

Several studies have shown the improvement of mechanical properties and biological activity of PLA scaffolds generated by FDM [71,72]. Different fillers were used in compression [73] and flexural studies [74], but to the best of our knowledge, the mechanical properties of PLA-based nanocomposites were never investigated by tensile strength analysis. Overall, our findings indicate that GO is a promising filler for improving the mechanical properties of biopolymers made by FDM.

### 3.6. Biological studies

The scaffold biocompatibility was then investigated using MG-63 cells that were derived from a human bone osteosarcoma and exhibit osteogenic potential (Fig. 6a). Compared with cells grown without scaffolds (control), the statistical analysis showed a higher viability of the cells in the presence of PLA and PLA/GO independently of GO percentages. No significant differences (ns in the figure) were observed between the samples with 0.1 and 0.2% meaning that the addition of GO had no influence on the viability of the cells. These results suggest that GO incorporation as nanofiller for PLA is biocompatible.

MC3T3-E1 cells were used to confirm the biocompatibility of the scaffolds (Fig. 6b). After 4 days of culture, no significant differences were observed between control and the scaffolds. After 7 days of

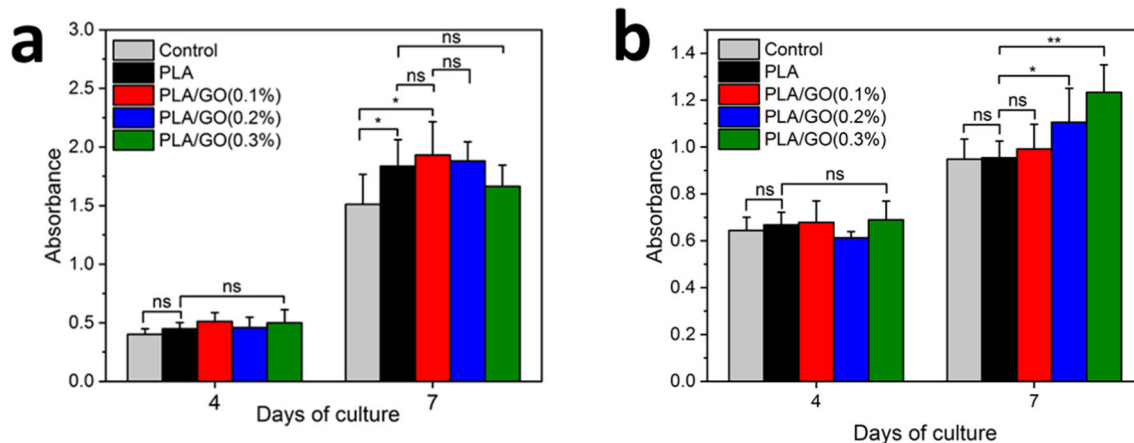


**Fig. 6.** (a) MG-63 and (b) MC3T3-E1 cell viability when cultured in the presence of PLA and PLA/GO nanocomposite scaffolds was assessed with the MTT assay at day 4 and 7 after seeding (ns = not significant).

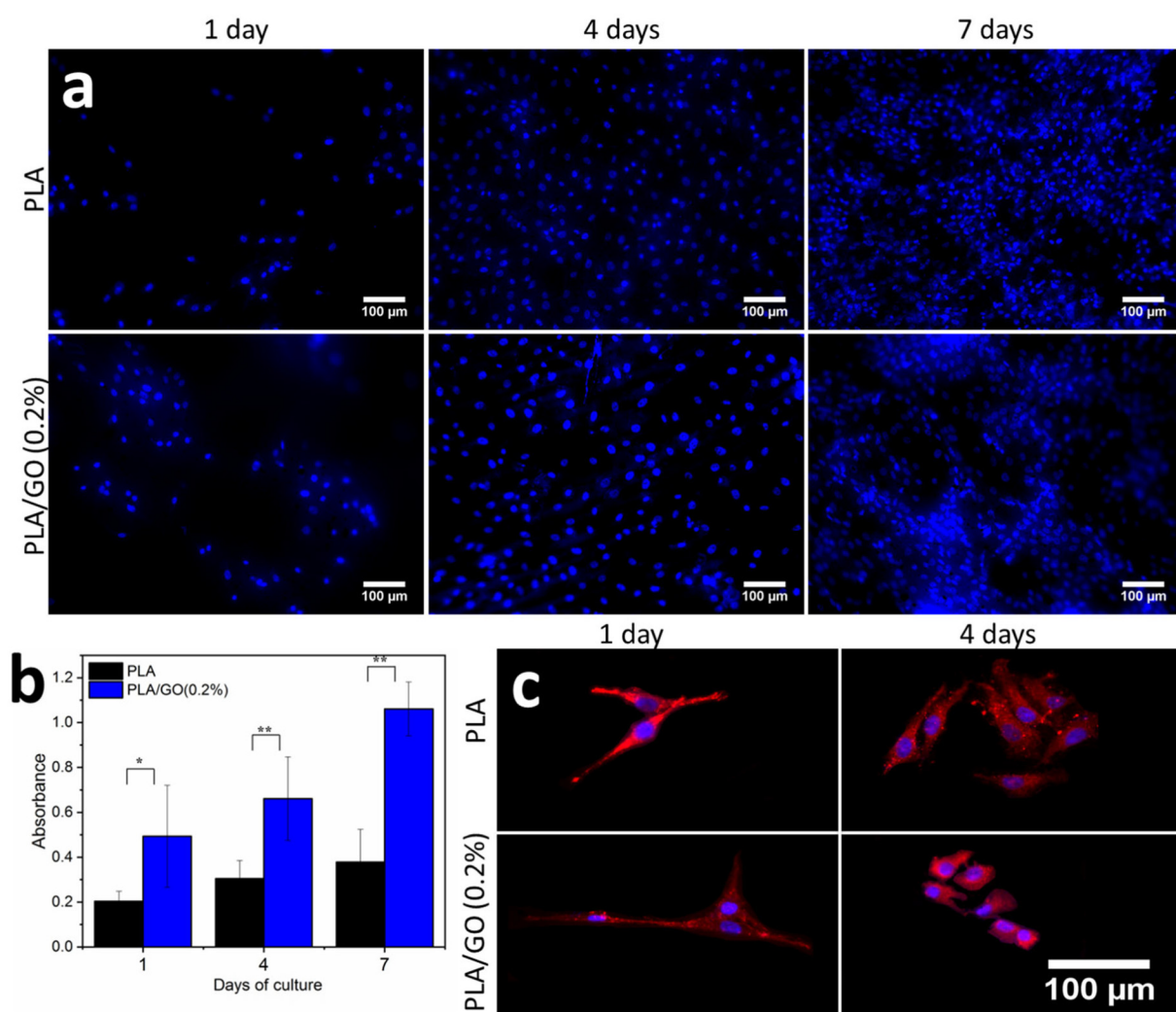


**Fig. 7.** MG-63 cell proliferation and attachment on PLA and PLA/GO nanocomposite scaffolds. (a) Analysis by DAPI staining of DNA (blue) of MG-63 cell proliferation on the PLA and PLA/GO scaffolds. (b) Cell proliferation monitoring using the MTT assay at different time points after seeding (ns = not significant, \* $p < 0.05$ , \*\* $p < 0.005$ ). (c) Actin immunodetection (red) and DAPI staining of DNA (blue) in a selected area of MG-63 cells attached on the PLA and PLA/GO scaffolds. (For interpretation of the references to colour in this figure legend, the reader is referred to the web version of this article.)

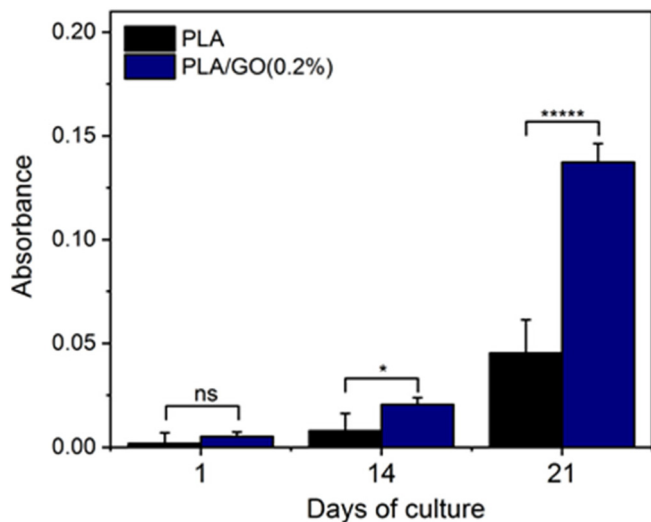


**Fig. 8.** MG-63 cell differentiation on PLA and PLA/GO scaffolds was evaluated using the Alizarin Red-S mineralization assay at different time points after switching to differentiation medium (ns = not significant, \* $p < 0.05$ ). (For interpretation of the references to colour in this figure legend, the reader is referred to the web version of this article.)

culture, higher viability was observed with addition of 0.2 and 0.3% GO. This suggests that the PLA/GO scaffolds enhanced the viability of these cells.

In some cases, biomaterials implantation in bone tissue may cause an inflammatory response due to the acidic microenvironment induced by the scaffold [75]. However, PLA is a stable polymer with a slow degradation rate which depends on polymer composition and on the tissue considered [76]. In this case PLA is relatively stable with  $< 1\%$  degradation after 25 days (Fig. S4). The introduction of GO will improve the degradation of PLA (Fig. S4). PLA scaffold does not induce high enough acidity in the microenvironment to have a major negative effect on cell behavior. The cells viability study confirmed that PLA does not induce any cytotoxicity.

Similarly, MG-63 cell proliferation on the two scaffolds was monitored first by staining cell nuclei with Hoechst 33342. This showed that cells readily proliferate on the scaffolds at 24 h, and reached confluency after 7 days of culture on the PLA and PLA/GO scaffolds (Fig. 7a). Cell proliferation quantification with the MTT assay at day 4 and 7 (Fig. 7b) confirmed these results and showed that GO incorporation promoted cell proliferation compared with scaffolds made only of PLA. Finally, cell attachment to the scaffolds was also analysed by staining cell nuclei with Hoechst 33342 and the cytoskeleton with an anti-actin antibody (Fig. 7c) which demonstrated that cells attached well on the PLA and PLA/GO scaffolds.

Finally, MG-63 cell mineralization was monitored by Alizarin Red-S staining at day 1, 14 and 21 after induction of differentiation. Colorimetric quantification of calcium deposition on the scaffolds by MG-63 cells (Fig. 8) showed that at day 21, it was increased by two-fold in samples with PLA/GO scaffolds compared with PLA scaffolds. This indicates that GO incorporation in the scaffold promotes mineralization. Altogether, these results demonstrate that PLA reinforced with 0.2% GO is biocompatible and may improve MG-63 cell mineralization activity.

#### 4. Conclusions

In conclusion, GO-reinforced PLA scaffolds were synthesized and thoroughly characterized, particularly their structural and mechanical properties and their biocompatibility. We successfully 3D printed PLA/GO nanocomposites with controlled morphology and a network of

interconnected pores around 300  $\mu\text{m}$ . Altogether, our results demonstrated that GO incorporation 1) increased the surface roughness and hydrophilicity, 2) did not modify the transition temperature, 3) decreased polymer crystallinity, 4) improved the mechanical properties of the scaffold, and 5) promoted bone cell attachment, proliferation and differentiation. Our data clearly indicate that PLA reinforcement with 0.2% GO might represent a good strategy to obtain 3D printed scaffolds with very attractive mechanical properties and bioactivity, thus providing a promising material that could be used for bone tissue engineering applications upon validation using appropriate *in vivo* models.

#### Author statement

Conceptualization, C. T., D. C., V. C., M. B.; methodology, H. B., S. N., C. T., D. C., V. C., M. B.; formal analysis, H. B., S. N., C. T., C. B., J. B.; data curation, H. B., S. N., C. T., C. B., J. B., S. B.; writing—original draft preparation, H. B., S. N.; writing—review and editing, H. B., S. N., C. T., J. B., S. B., H. G., V. H., D. C., V. C., M. B.; supervision, C. T., D. C., V. C., M. B.; project administration, V. C., M. B.; funding acquisition, V. C., M. B.

#### Declaration of competing interest

The authors declare that they do not have any conflict of interest.

#### Acknowledgment

We acknowledge the financial support from Indo-French Centre for the Promotion of Advanced Research-Cefipra (Project 5608-1), from CNRS (Project “Osez l’Interdisciplinarité: TraitCancer”) and from University of Montpellier (MUSE “3DTraitCancer”).

#### Appendix A. Supplementary data

Supplementary data to this article can be found online at <https://doi.org/10.1016/j.jmsec.2019.110595>.

#### References

- [1] D. Tang, et al., Biofabrication of bone tissue: approaches, challenges and translation for bone regeneration, *Biomaterials* 83 (2016) 363–382.
- [2] H.T. Aro, A.J. Aho, Clinical use of bone allografts, *Ann. Med.* 25 (1993) 403–412.
- [3] K. Rezwani, Q.Z. Chen, J.J. Blaker, A.R. Boccaccini, Biodegradable and bioactive porous polymer/inorganic composite scaffolds for bone tissue engineering, *Biomaterials* 27 (2006) 3413–3431.
- [4] S. Bose, M. Roy, A. Bandyopadhyay, Recent advances in bone tissue engineering scaffolds, *Trends Biotechnol.* 30 (2012) 546–554.
- [5] F.J. O’Brien, Biomaterials & scaffolds for tissue engineering, *Mater. Today* 14 (2011) 88–95.
- [6] A.J.R. Lasprilla, G.A.R. Martinez, B.H. Lunelli, A.L. Jardini, R. Maciel Filho, Poly-lactic acid synthesis for application in biomedical devices—a review, *Biotechnol. Adv.* 30 (2012) 321–328.
- [7] J. Muller, C. González-Martínez, A. Chiralt, Combination of poly(lactic acid) and starch for biodegradable food packaging, *Materials (Basel)* 10 (1–22) (2017).
- [8] D.E. Cutright, E.E. Hunsuck, Tissue reaction to the biodegradable polylactic acid suture, *Oral Surgery, Oral Med. Oral Pathol.* 31 (1971) 134–139.
- [9] R.R.M. Bos, et al., Degradation of and tissue reaction to biodegradable poly (L-lactide) for use as internal fixation of fractures: a study in rats, *Biomaterials* 12 (1991) 32–36.
- [10] K. Madhavan Nampoothiri, N.R. Nair, R.P. John, An overview of the recent developments in polylactide (PLA) research, *Bioresour. Technol.* 101 (2010) 8493–8501.
- [11] V. Karageorgiou, D. Kaplan, Porosity of 3D biomaterial scaffolds and osteogenesis, *Biomaterials* 26 (2005) 5474–5491.
- [12] B.Q. Chen, et al., Investigation of silk fibroin nanoparticle-decorated poly(L-lactide) composite scaffolds for osteoblast growth and differentiation, *Int. J. Nanomedicine* 12 (2017) 1877–1890.
- [13] H. Kim, A.A. Abdala, C.W. Macosko, Polymer nanocomposites with graphene, *Young*, 2010, pp. 1–13, <https://doi.org/10.1021/ma100572e>.
- [14] A.K. Geim, Graphene: Status and Prospects. 1530 (2010) 1530–1535.
- [15] S. Stankovich, et al., Graphene-based composite materials, *Nature* 442 (2006) 282–286.

- [16] Y. Zhu, et al., Graphene and graphene oxide: synthesis, properties, and applications, *Adv. Mater.* 22 (2010) 3906–3924.
- [17] W. Gao, **The chemistry of graphene oxide**, *Graphene Oxide Reduct. Recipes, Spectrosc. Appl.* (2015) 61–95, [https://doi.org/10.1007/978-3-319-15500-5\\_3](https://doi.org/10.1007/978-3-319-15500-5_3).
- [18] A.M. Pinto, et al., Biocompatibility of poly (lactic acid) with incorporated graphene-based materials, *Colloids Surfaces B Biointerfaces* 104 (2013) 229–238.
- [19] A.M. Pinto, J. Cabral, D.A.P. Tanaka, A.M. Mendes, F.D. Magalhães, Effect of incorporation of graphene oxide and graphene nanoplatelets on mechanical and gas permeability properties of poly (lactic acid) films, *Polym. Int.* 62 (2013) 33–40.
- [20] Q. Chen, et al., 3D printing biocompatible polyurethane/poly(lactic acid)/graphene oxide nanocomposites: anisotropic properties, *ACS Appl. Mater. Interfaces* 9 (2017) 4015–4023.
- [21] D.G. Papageorgiou, I.A. Kinloch, R.J. Young, Mechanical properties of graphene and graphene-based nanocomposites, *Prog. Mater. Sci.* 90 (2017) 75–127.
- [22] S.-R. Ryoo, et al., Biomedical applications of graphene and graphene oxide, *Acc. Chem. Res.* 46 (2013) 2211–2224.
- [23] S.S. Nanda, G.C. Papaefthymiou, D.K. Yi, Functionalization of graphene oxide and its biomedical applications, *Crit. Rev. Solid State Mater. Sci.* 40 (2015) 291–315.
- [24] R.K. Kankala, et al., Cardiac tissue engineering on the nanoscale, *ACS Biomaterials Science and Engineering* 4 (2018) 800–818.
- [25] E. Kolanthai, et al., Graphene oxide-a tool for the preparation of chemically crosslinking free alginate-chitosan-collagen scaffolds for bone tissue engineering, *ACS Appl. Mater. Interfaces* 10 (2018) 12441–12452.
- [26] C. Liao, et al., Fabrication of porous biodegradable polymer scaffolds using a solvent merging/particulate leaching method, *J. Biomed. Mater. Res. An Off. J. Soc. Biomater. Japanese Soc. Biomater. Aust. Soc. Biomater. Korean Soc. Biomater.* 59 (2002) 676–681.
- [27] N. Sultana, M. Wang, PHBV/PLLA-based composite scaffolds fabricated using an emulsion freezing/freeze-drying technique for bone tissue engineering: surface modification and in vitro biological evaluation, *Biofabrication* 4 (2012) 15003.
- [28] Y.X. Huang, J. Ren, C. Chen, T.B. Ren, X.Y. Zhou, Preparation and properties of poly (lactide-co-glycolide)(PLGA)/nano-hydroxyapatite (NHA) scaffolds by thermally induced phase separation and rabbit MSCs culture on scaffolds, *J. Biomater. Appl.* 22 (2008) 409–432.
- [29] S. Nagarajan, et al., Design of boron nitride/gelatin electrospun nanofibers for bone tissue engineering, *ACS Appl. Mater. Interfaces* 9 (2017) 33695–33706.
- [30] F.S. Senatov, et al., Mechanical properties and shape memory effect of 3D-printed PLA-based porous scaffolds, *J. Mech. Behav. Biomed. Mater.* 57 (2016) 139–148.
- [31] S. Gómez, M.D. Vlad, J. López, E. Fernández, Design and properties of 3D scaffolds for bone tissue engineering, *Acta Biomater.* 42 (2016) 341–350.
- [32] A. Rogina, et al., Macroporous poly(lactic acid) construct supporting the osteoinductive porous chitosan-based hydrogel for bone tissue engineering, *Polymer* 98 (2016) 172–181.
- [33] D.H. Rosenzweig, E. Carelli, T. Steffen, P. Jarzem, L. Haglund, 3D-printed ABS and PLA scaffolds for cartilage and nucleus pulposus tissue regeneration, *Int. J. Mol. Sci.* 16 (2015) 15118–15135.
- [34] R.K. Kankala, et al., Effect of Icarin on engineered 3D-printed porous scaffolds for cartilage repair, *Materials (Basel)* 11 (2018).
- [35] R.K. Kankala, X.M. Xu, C.G. Liu, A.Z. Chen, S.B. Wang, 3D-printing of microfibrillar porous scaffolds based on hybrid approaches for bone tissue engineering, *Polymers (Basel)* 10 (2018).
- [36] S. Bose, S. Vahabzadeh, A. Bandyopadhyay, Bone tissue engineering using 3D printing, *Mater. Today* 16 (2013) 496–504.
- [37] F.P.W. Melchels, J. Feijen, D.W. Grijpma, A review on stereolithography and its applications in biomedical engineering, *Biomaterials* 31 (2010) 6121–6130.
- [38] R. Gauvin, et al., Microfabrication of complex porous tissue engineering scaffolds using 3D projection stereolithography, *Biomaterials* 33 (2012) 3824–3834.
- [39] Y. Luo, A. Lode, A.R. Akkineni, M. Gelinsky, Concentrated gelatin/alginate composites for fabrication of predesigned scaffolds with a favorable cell response by 3D plotting, *RSC Adv.* 5 (2015) 43480–43488.
- [40] J.M. Williams, et al., Bone tissue engineering using polycaprolactone scaffolds fabricated via selective laser sintering, *Biomaterials* 26 (2005) 4817–4827.
- [41] S.V. Murphy, A. Atala, 3D bioprinting of tissues and organs, *Nat. Biotechnol.* 32 (2014) 773.
- [42] I. Zein, D.W. Hutmacher, K.C. Tan, S.H. Teoh, Fused deposition modeling of novel scaffold architectures for tissue engineering applications, *Biomaterials* 23 (2002) 1169–1185.
- [43] B.N. Turner, R. Strong, S.A. Gold, A review of melt extrusion additive manufacturing processes: I. Process design and modeling, *Rapid Prototyp. J.* 20 (2014) 192–204.
- [44] F. Ning, W. Cong, J. Qiu, J. Wei, S. Wang, Additive manufacturing of carbon fiber reinforced thermoplastic composites using fused deposition modeling, *Compos. Part B Eng.* 80 (2015) 369–378.
- [45] P.S.P. Poh, et al., Poly(lactides) in additive biomanufacturing, *Adv. Drug Deliv. Rev.* 107 (2016) 228–246.
- [46] T. Serra, J.A. Planell, M. Navarro, High-resolution PLA-based composite scaffolds via 3-D printing technology, *Acta Biomater.* 9 (2013) 5521–5530.
- [47] T. Serra, M.A. Mateos-Timoneda, J.A. Planell, M. Navarro, 3D printed PLA-based scaffolds: a versatile tool in regenerative medicine, *Organogenesis* 9 (2013) 239–244.
- [48] D.C. Marciano, et al., Improved synthesis of graphene oxide, *ACS Nano* 4 (2010) 4806–4814.
- [49] E.W. Fischer, H.J. Storz, G. Wegner, Investigation of the structure of solution grown crystals of lactide copolymers by means of chemical reactions, *Kolloid-Zeitschrift Zeitschrift Für Polym* 251 (1973) 980–990.
- [50] T.-L. Vu, J. Barés, Soft Grain Compression: Beyond the Jamming Point, (2019).
- [51] T.L. Vu, J. Barés, S. Mora, S. Nezamabadi, Deformation field in diametrically loaded soft cylinders, *Exp. Mech.* (2019), <https://doi.org/10.1007/s11340-019-00477-4>.
- [52] S.H. Lee, I.Y. Kim, W.S. Song, Biodegradation of polylactic acid (PLA) fibers using different enzymes, *Macromol. Res.* 22 (2014) 657–663.
- [53] K. Deshmukh, S.M. Khatake, G.M. Joshi, Surface properties of graphene oxide reinforced poly(vinyl chloride) nanocomposites, *J. Polym. Res.* 20 (2013).
- [54] Y. Arima, H. Iwata, Effect of wettability and surface functional groups on protein adsorption and cell adhesion using well-defined mixed self-assembled monolayers, *Biomaterials* 28 (2007) 3074–3082.
- [55] D.P. Dowling, I.S. Miller, M. Ardhauoi, W.M. Gallagher, Effect of surface wettability and topography on the adhesion of osteosarcoma cells on plasma-modified polystyrene, *J. Biomater. Appl.* 26 (2011) 327–347.
- [56] K. Webb, V. Hlady, P.A. Tresco, Relative importance of surface wettability and charged functional groups on NIH 3T3 fibroblast attachment, spreading, and cytoskeletal organization, *J. Biomed. Mater. Res.* 41 (1998) 422–430.
- [57] C. Zhang, et al., The surface grafting of graphene oxide with poly (ethylene glycol) as a reinforcement for poly (lactic acid) nanocomposite scaffolds for potential tissue engineering applications, *J. Mech. Behav. Biomed. Mater.* 53 (2016) 403–413.
- [58] J.M. Campos, A.M. Ferraria, A.M. Botelho Do Rego, M.R. Ribeiro, A. Barros-Timmons, Studies on PLA grafting onto graphene oxide and its effect on the ensuing composite films, *Mater. Chem. Phys.* 166 (2015) 122–132.
- [59] B. Wittbrodt, J.M. Pearce, The effects of PLA color on material properties of 3-D printed components, *Addit. Manuf.* 8 (2015) 110–116.
- [60] M. Gong, Q. Zhao, L. Dai, Y. Li, T. Jiang, Fabrication of polylactic acid/hydroxyapatite/graphene oxide composite and their thermal stability, hydrophobic and mechanical properties, *Journal of Asian Ceramic Societies* 5 (2017) 160–168.
- [61] S. Villar-Rodil, J.I. Paredes, A. Martínez-Alonso, J.M.D. Tascón, Preparation of graphene dispersions and graphene-polymer composites in organic media, *J. Mater. Chem.* 19 (2009) 3591–3593.
- [62] T. Ramanathan, et al., Functionalized graphene sheets for polymer nanocomposites, *Nat. Nanotechnol.* 3 (2008) 327–331.
- [63] Y. Xu, W. Hong, H. Bai, C. Li, G. Shi, Strong and ductile poly(vinyl alcohol)/graphene oxide composite films with a layered structure, *Carbon N. Y.* 47 (2009) 3538–3543.
- [64] Y. Shen, et al., Chemical and thermal reduction of graphene oxide and its electrically conductive polylactic acid nanocomposites, *Compos. Sci. Technol.* 72 (2012) 1430–1435.
- [65] M.S. Huda, M. Yasui, N. Mohri, T. Fujimura, Y. Kimura, Dynamic mechanical properties of solution-cast poly(L-lactide) films, *Mater. Sci. Eng. A* 333 (2002) 98–105.
- [66] P. Ravi, P.S. Shiakolas, T.R. Welch, Poly-L-lactide acid: pellets to fiber to fused filament fabricated scaffolds, and scaffold weight loss study, *Addit. Manuf.* 16 (2017) 167–176.
- [67] K.H. Liao, S. Aoyama, A.A. Abdala, C. Mocosko, Does graphene change T g of nanocomposites? *Macromolecules* 47 (2014) 8311–8319.
- [68] H.-D. Huang, et al., Improved barrier properties of poly (lactic acid) with randomly dispersed graphene oxide nanosheets, *J. Memb. Sci.* 464 (2014) 110–118.
- [69] Z. Xu, et al., Morphology, rheology and crystallization behavior of polylactide composites prepared through addition of five-armed star polylactide grafted multiwalled carbon nanotubes, *Polymer (Guildf)* 51 (2010) 730–737.
- [70] Y. Song, et al., Measurements of the mechanical response of unidirectional 3D-printed PLA, *Mater. Des.* 123 (2017) 154–164.
- [71] A. Grémare, et al., Characterization of printed PLA scaffolds for bone tissue engineering, *J. Biomed. Mater. Res. - Part A* 106 (2018) 887–894.
- [72] A. Gregor, et al., Designing of PLA scaffolds for bone tissue replacement fabricated by ordinary commercial 3D printer, *J. Biol. Eng.* 11 (2017) 1–21.
- [73] C. Esposito Corcione, et al., Highly loaded hydroxyapatite/microsphere/PLA porous scaffolds obtained by fused deposition modelling, *Ceram. Int.* 45 (2019) 2803–2810.
- [74] C.E. Corcione, et al., 3D printing of hydroxyapatite polymer-based composites for bone tissue engineering, *J. Polym. Eng.* 37 (2017) 741–746.
- [75] R.K. Kankala, et al., Highly porous microcarriers for minimally invasive in situ skeletal muscle cell delivery, *Small* 15 (2019).
- [76] D. da Silva, et al., Biocompatibility, biodegradation and excretion of polylactic acid (PLA) in medical implants and theranostic systems, *Chem. Eng. J.* 340 (2018) 9–14.